Direct Integration of Functional Structures on 3-D Microscale Surfaces by Laser Dynamic Forming

Huang Gao, Rui Tang, Teng Ma, Hanqing Jiang, Hongyu Yu, and Gary J. Cheng

***Abstract*—This paper demonstrates the scalable and fast-shaping top-down integration capability of laser dynamic forming (LDF), transferring functional structures conformal to three-dimensional (3-D) micro-to-mesoscale curvilinear features on various substrates by the laser-induced shockwave. The functional materials preserve their electrical resistance and temperature coefficient of resistance after the laser shock induced transfer. The ductile interconnections inherit 3-D microscale structures on various substrates without excessive necking and fracture. This process is realized by the lamination of functional materials with cushion layers and the shockwave controlled by laser pulse intensity. The ability of direct transfer is affected by the laser intensity, cushion layer thickness, and geometry of the 3-D substrates. The experiments and numerical study reveal that the cushion layer absorbs most of shockwave energy by large thickness reduction and extends the formability of ductile interconnections. Eventually, the thickness of ductile functional materials is distributed uniformly along the 3-D surfaces. The ranges of the processing conditions for direct integration of functional materials without property degradation are also investigated. [2013-0058]**

***Index Terms*—Direct integration, functional devices, laser shock, transfer, thin film.**

I. Introduction

THE expanding applications of micro-to-mesoscale electromechanical systems, such as artificial human implant [1], sensory skins for robotics [2], and flexible solar cells [3], call for the packaging and integration of heterogeneous materials and components with three-dimensional (3-D) surfaces, which are usually incompatible in a monolithic fabrication approach. Although current lithography-based technologies are very successful in fabricating high-performance, rigid and brittle devices on planar semiconductor substrates, there exists significant challenges in the fabrication and assembly of these devices on irregular and curvilinear 3-D surfaces without compromise in performance and efficiency. Various techniques have been developed to manufacture 3-D patterned microscale structures of both inorganic and polymeric materials, such as 3-D lithographic patterning [4], guided self-assembly [5], inkjet printing [6], and soft-lithographic-based fabrication [7]. However, these methods are time consuming and limited in throughput. To address these challenges, direct templating techniques have been developed to replicate or transfer 3-D patterns from master template to relatively softer materials, such as nanoimprint lithography [9] and detachment lithography [9], [10]. Nanoimprint lithography achieves 3-D patterns either by multistep overlapping [11] or by inclined imprinting [12]. In detachment lithography, the network of brittle devices connected by ductile bridges is transferred from Si wafer to prestrained planar surface, then to the final 3-D surface. The multistage transfer, the selective bonding and the specifically designed interconnection bridges, result in low yield and limit its mass production capabilities. There is a need to develop scalable and fast-shaping techniques that can manufacture microelectromechanical system (MEMS) devices on curvilinear 3-D surfaces efficiently, with a wide spectrum of functional materials.

Recently, laser dynamic forming (LDF) has been demonstrated its capability to deform polycrystalline metals on various 3-D substrates by laser shock induced pressure [13]. Due to high precision and repeatability, fast setup and superb flexibility, it has the potential in large area electronics fabrication. This paper will address its capability to directly integrate MEMS on 3-D surface. In order to preserve MEMS functions, the functional materials are encapsulated by polymer layers, which absorb most of the shock energy and minimize the defects in functional materials. The laser pulse energy and the shockwave pressure are also controlled in a range to achieve the shaping conformal to 3-D surfaces without degrading the functionality of the structures. The process mechanism of direct integration by LDF on uneven 3-D surfaces will be studied. The functionality of the device after transferring will be characterized. The effects of process conditions on these structures will be investigated by experiments and numerical simulations.

Manuscript received November 18, 2012; accepted April 4, 2013. Date of publication July 3, 2013; date of current version November 25, 2013. This work was supported in part by an NSF CAREER Award (CMMI-0547636), the NSF under Grant CMMI-0928752 through the program of Materials Processing and Manufacturing, and NSF CMMI-0700440. Subject Editor K. F. Bohringer. *(Corresponding author: G. J. Cheng. H. Gao and R. Tang contributed equally to this paper.)*

H. Gao and G. J. Cheng are with the School of Industrial Engineering, Purdue University, West Lafayette, IN 47906 USA (e-mail: gjcheng@purdue.edu; gao7@purdue.edu).

R. Tang is with the School of Electrical, Computer and Energy Engineering, Arizona State University, Tempe, AZ 85287 USA (e-mail: Rui.Tang.1@asu.edu).

H. Yu is with the School of Electrical, Computer and Energy Engineering and the School of Earth and Space Exploration, Arizona State University, Tempe, AZ 85287 USA (e-mail: hongyuyu@asu.edu).

T. Ma and H. Jiang are with the School for Engineering of Matter, Transport and Energy, Arizona State University, Tempe, AZ 85287 USA (e-mail: Teng.Ma.1@asu.edu; Hanqing.Jiang@asu.edu).

Color versions of one or more of the figures in this paper are available online at http://ieeexplore.ieee.org.

Digital Object Identifier 10.1109/JMEMS.2013.2262602

1057-7157 © 2013 IEEE

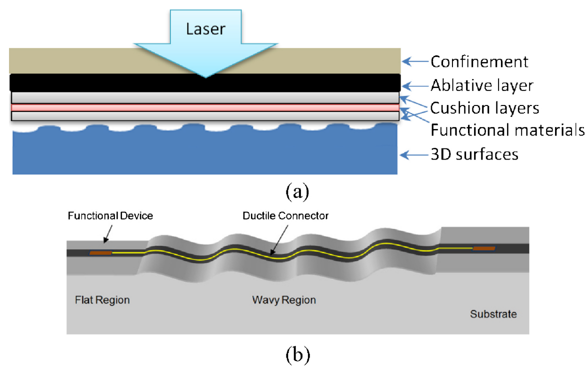

Fig. 1. Schematic setup of laser dynamic forming process to manufacture functional structure on 3-D microscale surface. (b) Controlled fabrication of laminated structure on 3-D patterned surface.

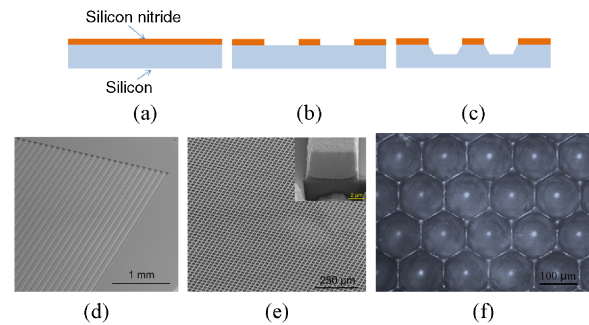

Fig. 2. Fabrication process of Si micropatterns by photolithography. (a) LPCVD of silicon nitride layer (0.6 μm thick). (b) Patterning of silicon nitride layer. (c) Anisotropic wet etching of silicon substrate. (d) The SEM image of the microgrooves in Si wafer fabricated by the processes in (a)–(c). (e) The SEM of a TEM grid bonded with Si wafer and the inserted SEM showing the cross-section of a grid bar (bar width:6.0 μm, bar height: 4.4 μm). (f) The SEM image of a polyglass microlens with an array of concave pyramids shape, with its side length of 80 μm and the depth of 44 μm.

II. Process Scheme

The process scheme of direct integration of functional structures on 3-D microscale surfaces is illustrated in Fig. 1(a). The laser pulse transmits through confinement layer, such as glass slide, and irradiates ablation layer into plasma plume. Constrained by the confinement, the plasma turns into a shockwave propagating through the laminated layers consisting of cushion layers and functional materials. The laser shock induced pressure will propagate to the laminated layers and shape them conformally onto the underlying 3-D surfaces. The cushion layers function as the shock loading absorber and load transfer medium for the functional layer. The functional materials are transferred to 3-D surfaces uniformly in nanoseconds. Compared to other multiple-stage transfer technologies, this method eliminates the need to fabricate inverted molds for surface replication, which could be costly and infeasible at the microscale. Since the shockwave pressure is primarily determined by the applied laser intensity per Fabbro's model [14], the laser pulse energy could be optimized for different functional materials and substrates to preserve the proper function of fabricated devices and achieve conformal shaping. The load being transferred to the functional materials is much less than the shock pressure due to the cushion layer, the thickness of which could also be tuned to control the load transfer. This technology provides much flexibility and selectivity in assembly location and area since the scanning speed, focal plane and coordinates of laser beam are readily adjusted by optical configurations and the motorized $X-Y-Z$ translation stage. Fig. 1(b) schematically shows a way to control plastic deformation of functional materials by the patterned 3-D surface to allow different regions (fragile devices and ductile connections) to experience different deformations during LDF. It is expected that metallic connections aligned to wavy regions will have moderate plastic deformation, while the devices aligned with flat regions will have minimal plastic deformation.

III. Experimental and Simulation Methods

A. Preparation of 3-D Microscale Patterns on Various Substrates

The microscale patterns have been proved to be effective in changing the biocompatibility [22], [23] and hydrophobicity [24], light absorption and reflection [25]. The diversified applications also require the functional materials and devices that can be readily transplanted or transformed to 3-D-patterned substrates of different materials. In this paper, regular and irregular 3-D microscale patterns were provided by three substrates of materials which were widely used in MEMS: Si wafer, polycarbonate (PC), and metals.

One way to introduce large areas of micropatterns to Si wafer is photolithography and etching. The fabrication process of micropatterns in Si wafer is shown in Figs. 2(a)–(c). A 0.6 μm thick silicon nitride layer on the top surface of silicon substrate was deposited by low pressure chemical vapor deposition (LPCVD). Silicon nitride was patterned by photoresist and removed selectively by reactive ion etching. The Si wafer was wet and etched by KOH. Fig. 2(d) shows the SEM of microscale patterns in silicon by focused ion beam lithography/scanning electron microscopy (FIB/SEM). Another type of large area micropatterns on Si wafer was realized by copper SPI Slim-Bar® TEM Grids, as shown in Fig. 2(e). The TEM grids were bonded with Si wafer by spin-coated photoresist: 950PMMA A4 (Microchem Corp.). The dimension of holes and bars varied from 6.4 to 54 μm and 4.4 to 19 μm, respectively. Fig. 2(f) demonstrates the top view of a polyglass microlens, consists of an array of concave pyramids with a side length of 80 μm and a height of 44 μm. PC is widely used in micro-optics due to good transparency in the visible wavelengths, high optical absorbance in the deep-UV wavelength band, and thermal stability. In this paper, micropatterns on PC are fabricated via deep-UV pulsed laser interference ablation. Microlens array is one of the most critical micro-optics elements widely used in laser diode array collimators, camera autofocus systems, light-emitting diode print bars, and 3-D optical switches. Finally, coins provide irregular 3-D patterns on metallic surfaces for this paper. A thin photoresist layer, PMMA A4 or SU-8 2002 (Microchem Corp.), was spin-coated on these substrates or laminated thin films to act as an adhesion promoter in the assembly.

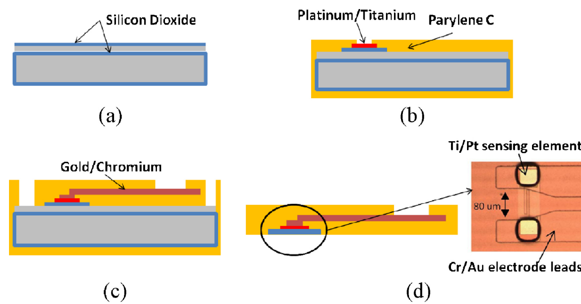

Fig. 3. Sensor fabrication process: (a) Dry thermal growth of SiO_2 and deposition of a sacrificial Si layer using electron-beam evaporator and then dry thermal growth of another SiO2 layer; (b) deposition and patterning of Ti/Pt as a sensing element, followed by deposition and patterning of the first parylene-C layer; (c) deposition and patterning of Cr/Au for the electrode leads and the second parylene-C layer; and (d) etching of Si sacrificial layer underneath to release the sensor leading to the final device.

B. Laminated Functional Materials and Devices

One of the keys to transfer functional structures on 3-D surfaces is to encapsulate them in a soft polymer material as cushion layers. Parylene-C is chosen to provide mechanical protection and enhanced lubricity during transfer with good electrical insulation, moisture and chemical isolation. The functional materials include brittle materials in the sensor devices, such as SiO_2, and ductile materials in the wiring connections, such as Au/Cr. Fig. 3 illustrates the fabrication processes of the temperature sensor, which are 4 cm in length, 340 μm in width, and 17 μm in thickness [26]. Detailed fabrication processes include: 1) SiO_2 was grown on silicon substrate through dry thermal oxidation (1100 °C) and then a sacrificial Si layer was deposited using electron-beam evaporator, followed by dry thermal growth of another SiO_2 layer; 2) double-layer metals Ti/Pt (50 nm/100 nm) were deposited and patterned to form sensing elements, followed by the conformal coating of first parylene-C layer; 3) Cr/Au (20 nm/600 nm) were deposited and patterned for the electrode leads and another layer of parylene-C layer was coated and patterned; and 4) etching of Si sacrificial layer underneath to release the sensor leading to the final device. Since ductile materials in the wiring connections experience more plastic deformations than the sensing components, parylene laminated thin film was fabricated in order to investigate the deformation characteristics of ductile connections under various conditions of laser intensities and microscale 3-D substrates. The laminated thin film consists of a thin metallic layer (Cr/Au) sandwiched by the two layers of parylene.

C. Microstructure Characterization in SEM/FIB

During LDF, the cushion layer absorbs most of the shockwave energy by significant thickness change to protect functional materials from excessive deformation and fracture, and transfer the controlled pressure to the functional materials in order to conformally integrate them onto the 3-D surfaces. In this paper, the functional structures were characterized along the FIB-fabricated cross section to verify this assumption. The samples were tilted to 52° so that the gallium ion beam was perpendicular to the sample surface to prepare the cross section.

D. Property Characterization of Functional Structures

The temperature sensor consists of a resistor (Ti/Pt) with resistance varied with temperature. To experimentally demonstrate the proper working of the functional structure, the electrical resistance (at room temperature 23 °C) and the temperature coefficient of resistance (TCR) was measured before and after the direct transfer with LDF. The measurement was operated on a probe station (The Micromanipulator Co., Inc.) connected with Agilent 4155C Semiconductor Parameter Analyzer. The resistance of the temperature sensor was obtained at several temperatures, from 23 °C to 83 °C with increment of 10 °C.

E. Finite Element Methods

The understanding of dynamic deformation behaviors of functional laminated films and the stress–strain distribution across the heterogeneous materials is important to the reliable design and service, especially when impulse loadings are involved.

As one of semicrystalline polymers, parylene is characterized by the morphology of the crystalline regions of ordered lamellae, surrounded by the amorphous regions of unordered molecular chains. It is the interactions and behavior of these structures that account for the complex deformation behavior of parylene. Two main approaches have been taken to develop material constitutive models for the semicrystalline polymers. The first is the physically micromechanical model where the stress–strain relationship is considered on the basis of thermodynamic activation of molecules. The second is a phenomenological one where the stress–strain relationship is modeled by fitting experimental data of representative volumes of material. Although the physically based constitutive models are fundamental to understand the micro- and macroscopic deformation mechanisms of polymers, they generally have very complex form including a series of complicated equations. They could produce the fair agreement with experimental observation in the small strain region but failed when extrapolating to the macroscopic scale because semicrystalline polymers have highly anisotropic microstructures. Hence, in numerical simulations the preferable model is the phenomenological one due to its simplicity and efficient algorithms on the large scale. In this paper, the phenomenological model proposed by G'Sell and Jonas is simplified to consider the plastic strain-hardening and strain rate dependence of viscous behavior of a semicrystalline polymer [27], without the items to describe the initial non-linear elastic behavior.

$$\sigma = Ke^{h\varepsilon^2}(\dot{\varepsilon})^m e^{\frac{\alpha}{T}}$$

where $\sigma$is the equivalent stress, $\varepsilon$is the equivalent strain, $\dot{\varepsilon}$is the equivalent strain rate, T is the absolute temperature, and K, α, h, and m are the material coefficients. The function $e^{h\varepsilon^2}$describes a plastic strain hardening, and $(\dot{\varepsilon})^m$ describes a viscous behavior. The parameters' values are estimated to approximate the deformation morphologies of parylene layers due to the lack of experimental measurements of parylene films at ultrahigh strain rates.

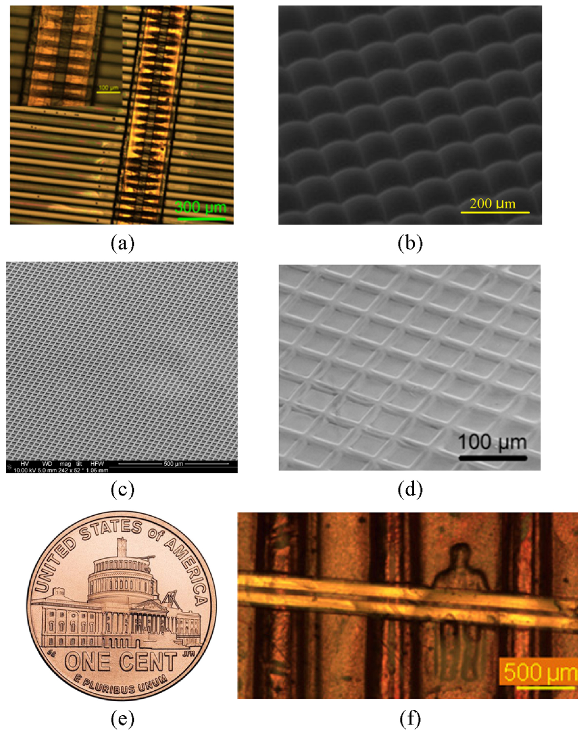

Fig. 4. A optical image of functional structures conformal to the micropatterns in a Si wafer, which are bonded together by a spin-coated PMMA A4. Laser intensity: 0.18 GW/cm^2, beam size: 4 mm. (b) The 3-D microscale patterns of laminated thin film inherited from microlens arrays. Laser intensity: 0.21 GW/cm^2, beam size: 4 mm. The 3-D microscale patterns (c) of laminated thin film inherited from TEM mesh (d). Laser intensity: 0.21 GW/cm^2, beam size: 4 mm. (e) The optical image of one U.S. cent. (f) The optical image of mesoscale 3-D structures on the surface of one cent, which are bonded together by spin-coated SU-8 3005. Laser intensity: 0.18 GW/cm^2, beam size: 6 mm.

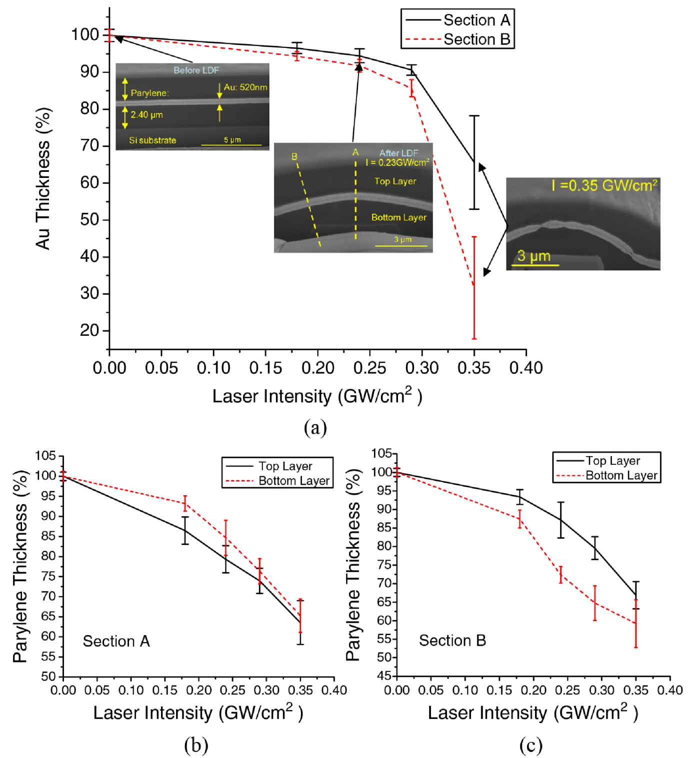

Fig. 5. The thickness reduction of Au layer at the top and corner of the grid bar, with the cross sections of laminated thin film before and after LDF; and (b) and (c) the thickness reduction of top and bottom of the parylene layer at two sections.

The dynamic/explicit module in ABAQUS (Version 6.8) was chosen in the simulation for its wide applications in the high-strain-rate loading. The temporal history of shockwave pressure was defined by Fabbro's model and input into ABAQUS by the subroutine DLOAD.

IV. Results and Analysis

A. *Direct Transfer on Three Types of Surfaces and Device Performance*

The results on conformal transfer of the functional materials on 3-D surfaces of different substrates are shown in Fig. 4. In Fig. 4(a), a temperature sensor acquired the deformation defined by regular micropatterns on Si wafer. The ductile wire connection was selectively deformed above micropatterns while the functional sensing part was aligned with the flat regions to experience minimal plastic deformation. The laser intensity was controlled to avoid excessive compression and necking of functional material. The sensor resistivity changed from 1.18 kΩ to 1.19 kΩ after LDF and TCR was kept unchanged at approximately 0.11%/ °C. It directly proves that LDF is a feasible solution to produce 3-D microscale structures and preserve the proper functioning of the fabricated devices by controlled plastic deformation. The regular micropatterns on Si wafer were replaced by the mesoscale patterns on coins to demonstrate the scalability of LDF. In Fig. 4(f), another temperature sensor was deformed compliantly on mesoscale pillars of a U.S. coin. The sensor resistivity changed from 1.35 kΩ to 1.42 kΩ after LDF and TCR was unchanged at approximately 0.12%/ °C, which indicated that the deformation was controlled to prevent the fracture of functional layer. The scalability of LDF is realized by increasing laser beam size and pulse energy to achieve the same laser intensity over a larger area.

B. *Processing Mechanisms of Direct Transfer by LDF*

The effects of laser intensity on functional materials are shown in Fig. 5. The as-received 5 μm thick laminated thin film was deformed on top of TEM mesh grid (G1000HS) by the increased laser intensities. The thickness changes of Au and parylene layer at the top (Section A) and corner (Section B) of grid bar were measured in FIB/SEM and normalized in Fig. 5. In general, the thicknesses of all materials decreased with laser intensities. But there are some remarkable differences between Au and parylene in the deformation behaviors. While there was significant thickness reduction in parylene throughout all the laser intensities, Au layer only experienced a small amount of attenuation by low and moderate laser intensities. At high laser intensities, the excessive shockwave energy induced the delamination between Au and parylene, which again lead to the drastic necking and fracture of Au layer. The variances of Au and parylene thickness also increased at high laser intensities as the location and magnitude of necking initiation became more

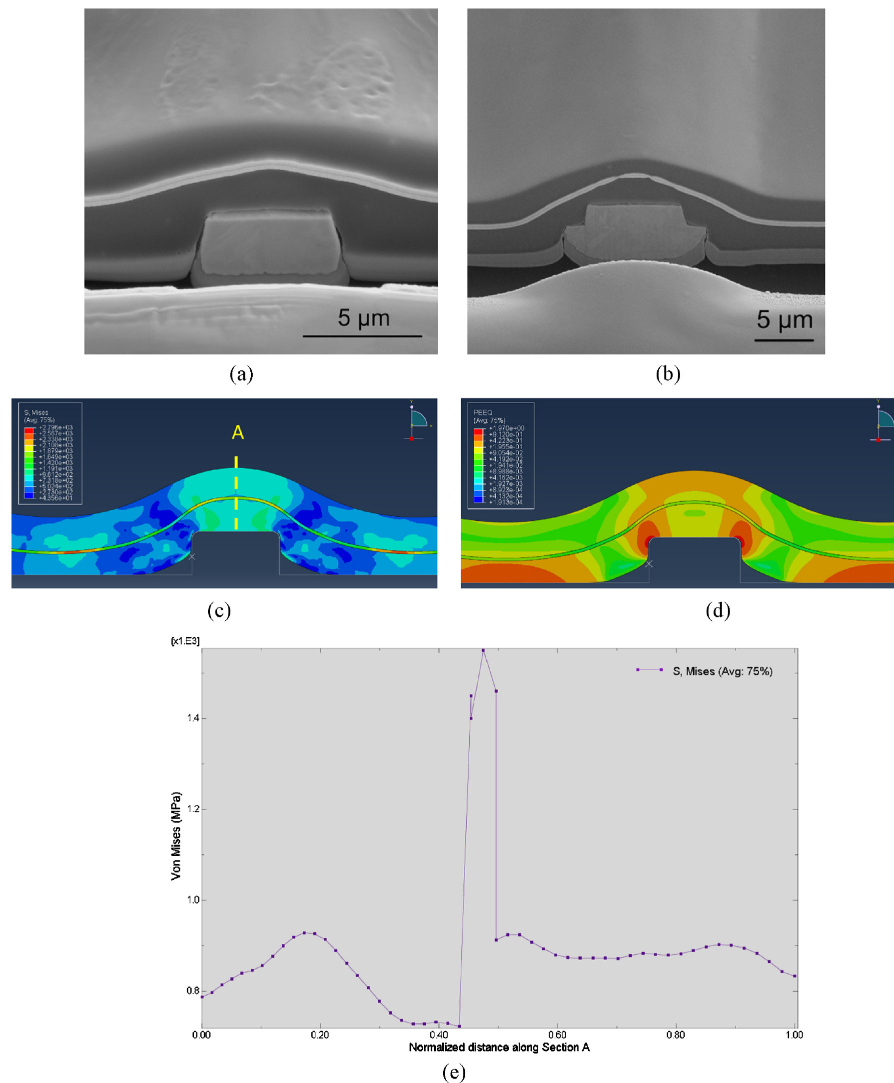

Fig. 6. The FIB/SEM images of cross sections of a laminated thin film deformed on G1000HS Mesh Grid (a) and G400HS Mesh Grid (b). The sample was tilted at 52° in (a) and 40° in (b). (FEM results show the spatial distribution of the plastic stress (c) and strain (d) in the deformed functional structure in (a). (e) The stress discontinuity along section A in (c).

unpredictable. According to Fabbro's model, the shockwave pressure increases proportionally to the square root of applied laser intensity approximately. When the shockwave propagates through the laminated materials, the steeply rising shockwave front induces viscoelastic compression and acceleration to material velocity instantaneously, followed by a second stage of slower viscoplastic compression and viscous relaxation. Compared with the functional materials, parylene is more compressible because in semicrystalline polymers, densities of amorphous organic polymers are typically lower than that of the crystalline regions of ordered lamellae. The shear stress in the shock front exceeds the strength of the parylene, so that its bulk and shear moduli are reduced and it becomes more compressible. In the second viscous relaxation stage, shear relaxation and volume relaxation coexist when the polymer chains go over barriers to pack tighter and result in plastic deformations [15]. After shockwave unloading, since some of polymer chains remain trapped in a partially densified state, only part of the polymer volume recovers. That is, the majority of shockwave energy is converted to strain energy stored in the parylene, which will also be characterized in the finite element method (FEM). As shock compression by an instantaneous front is an irreversible adiabatic process with associated entropy increase, the laser intensity must be controlled to minimize the microstructural defects and avoid voids, delamination and excessive necking in functional materials.

Figs. 5(b) and (c) show the thickness change of the top and bottom parylene layer at the top and corner of the grid bar due to the different local deformation behaviors. At the top of the grid bar (Section A), the materials underwent the shockwave compression primarily. The top layer had more thickness reduction than the bottom layer since the shockwave was at its peak on the top surface and decayed through the propagation direction. On the other hand, at the bar corner (Section B), the materials were not only compressed, but also bended and stretched more severely when the deformation curvature decreased near the grid bar. That is why the bottom layer thickness was more reduced than the top layer at Section B.

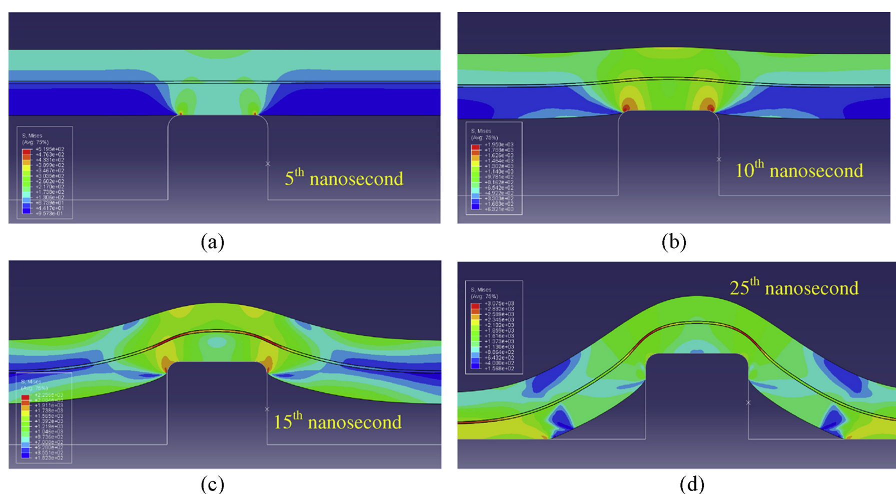

(a) (b) (c) (d)

Fig. 7. The deformation morphologies and stress distribution in the laminated film during four critical stages. Laser intensity: 0.20 GW/cm^2, parylene thickness: 2.4 μm on both sides, Au thickness: 0.2 μm, mold depth: 6.7 μm, bar width: 6 μm, and hole width: 54 μm.

C. Comparison of Experiment and Simulation Results

The ability of direct transfer of functional structures by LDF depends not only on the applied laser intensity and parylene thickness, but also on the size and aspect ratio of microscale substrates. As shown in Figs. 6(a) and (b), when the thickness of Slim-Bar TEM Grids, i.e., the height of the grid bar, increased from 3.6 μm to 6.7 μm, Au layer in the laminated film experienced excessive necking at the top or corner of the grid bar due to the localized intensive stretching and bending, which could possibly lead to functional degradation. The total plastic strain in Au layer reached more than 10% in this paper. It has been reported that if the metallic connections are freestanding, the rupture strain and aspect ratio are very small due to low hardening capability and formability at low strain rates [16], [17]. On the other hand, when metallic connections are well deposited on a polymer substrate, they could sustain strains up to a few tens of percent without appreciable cracks since the localized necking could be suppressed by the adherent substrate [18]–[21].

In this paper, three mechanisms facilitate direct transfer functional layer on 3-D surfaces. First, the functional layer was encapsulated by two parylene layers. The parylene layer not only allows functional material to sustain large plastic strain, but also provides compliant media between functional layer and sharp microfeatures to mitigate the localized intensive deformation. The load transferred to the functional materials is relatively much more uniformed as the parylene layer absorbs most of laser-induced shockwave energy upfront. Second, the through-thickness compressive shockwave suppresses the debonding between functional materials and cushion layer. Finally, the ductile materials have much better formability at high strain rate forming, due to delayed necking and inertia effect [13]. As a result, the interconnecting Au layer reached more than 10% strain in this paper.

The experimental conditions in Fig. 6(a) were incorporated in a finite element simulation. Figs. 6(c) and (d) illustrate the distribution of Von Mises and total plastic strain in the deformed structure. It shows that the intensive strains concentrate mostly in the parylene layer, other than the functional connection layer, especially at the top and corner of microgrid. The thickness of the parylene layer could be selected to provide maximum protection and prevent functional layer from crack and failure. Along the through-thickness direction, such as at section A, the stress distribution is discontinuous because the heterogeneous materials, Au and parylene, are of different in the dynamic constitutive behavior while they are connected by tie constraint to avoid relative motions in the model. This stress discontinuity, as illustrated in Fig. 6(e), tends to increase with the applied laser intensity, i.e., the shockwave energy. The results also reveal the existence of the shear stress along the interface between Au and parylene layers. When the shear stress exceeds the bonding strength of Au layer, the de-lamination occurs and triggers the premature fracture of Au layer. It was also observed in experiments that under similar laser conditions, there was only very mild thickness reduction in Au layer while parylene thickness was reduced significantly. After dynamic deformation, some of the shockwave energy is converted and stored as total strain energy in the materials. Assuming the volume of each material is kept constant, it reveals by FEM simulations that the about 97% of total strain energy is stored in the parylene and the average density of total strain energy in Au layer is only approximately 75% of that in the parylene layer. The lower level of strain energy density in functional layer helps to preserve the functions in the long run and future transfer the deformed functional structures.

D. Deformation Process During Shock Induced Transfer on 3-D Surface

Based on the simulation of shockwave pressure history, the laser intensity and the shock pressure reach their peaks at the 10th ns and the 11th–12th ns, respectively. The overall plastic deformation completes in tens of nanoseconds due to material inertia and shockwave propagation. The deformation process could be roughly divided into four stages, in which

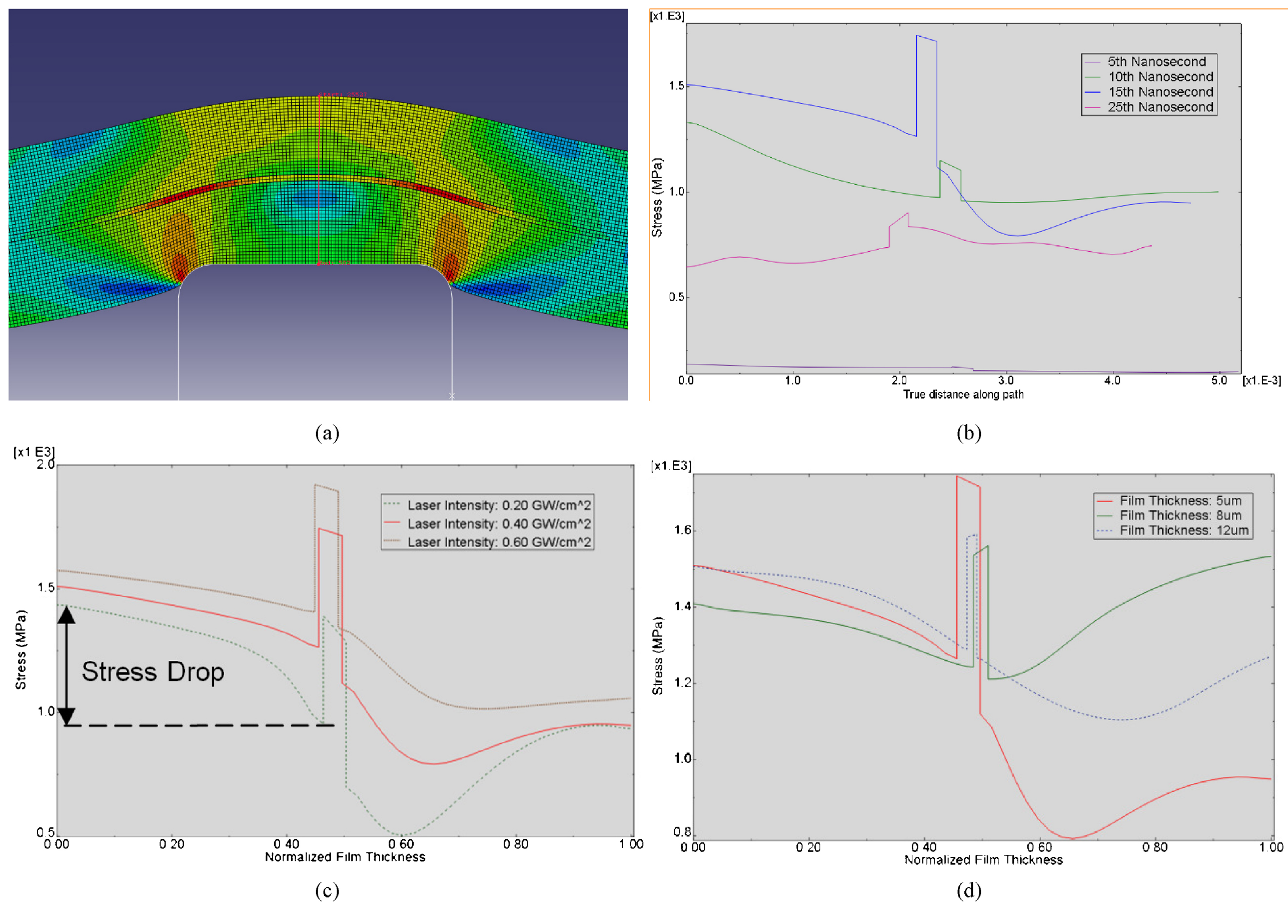

Fig. 8. The location of cross section to produce spatial distribution of Von Mises. (b) The temporal history of Von Mises along the cross section. Laser intensity: 0.20 GW/cm^2, parylene thickness: 2.4 μm, Au thickness: 0.2 μm. (c) The Von Mises profiles along the cross section under different laser intensity at 15th ns. The thickness of as-received laminated film is 5 μm. The overall thickness of deformed laminated film has been normalized. (d) The Von Mises profiles across the cross section with different parylene thicknesses at 15th ns. The overall thickness of deformed laminated film has been normalized.

the stress distribution of each stage is illustrated in Fig. 7. In the first 5 ns, the plasma shock pressure propagates through the laminated film, however, without any observable plastic deformation. The max Von Mises stress occurs at the corner of micromold bar where the bulk plastic deformation initiates. From 5th ns to 10th ns, the shockwave pressure continues to increase and induces high stress concentration in the lower parylene layer due to bending and compression. This high stress concentration in the parylene gradually propagates into functional layer (Au) and introduces the stress discontinuity across the interface of parylene and Au layer due to the different dynamic strengths. At 15th ns, the material at the bar corner is subject to significant bending and stretching simultaneously. The Von Mises in the functional layer and the stress discontinuity continue to increase to their maximum before laminated film collides with micromold bottom, which could potentially induce delamination and fracture of functional layer. That is why the depth and aspect ratio of micromold are critical to the formability of laminated film while preserving its functions. The laminated film will eventually collide with the micromolded bottom, followed by stress relaxation as the shockwave diminishes, as illustrated in Fig. 7(d). It could be observed that the parylene layer not only absorbs most of the shockwave energy to minimize the thickness change of the functional layer, but also enlarges the actual curvature at the sharp microfeatures to reduce the stress concentration in the functional layer. The parylene also prevents Au layer from violent collision with micromold bottom.

E. Effects of Laser Intensity and Parylene Thickness

It has been found that the stress discontinuity along the parylene–Au interface is crucial to the delamination and function of Au layer. It is worthwhile to characterize its relationships with laser intensity and cushion layer thickness to facilitate the optimal design of the laminated structures. In Fig. 8(a), the cross section on the top of micromold bar is selected to compare the Von Mises of different loading times, applied laser intensities, and parylene film thicknesses. Fig. 8(b) shows the temporal history of stress across this cross section. In the beginning of deformation, until 10th ns, the stress change along the interface is rather insignificant when the parylene absorbs most of the shockwave energy and undergoes the majority of compressive plastic deformation. While the material on the top of micromold bar is subjected to significant bending and stretching simultaneously, not only

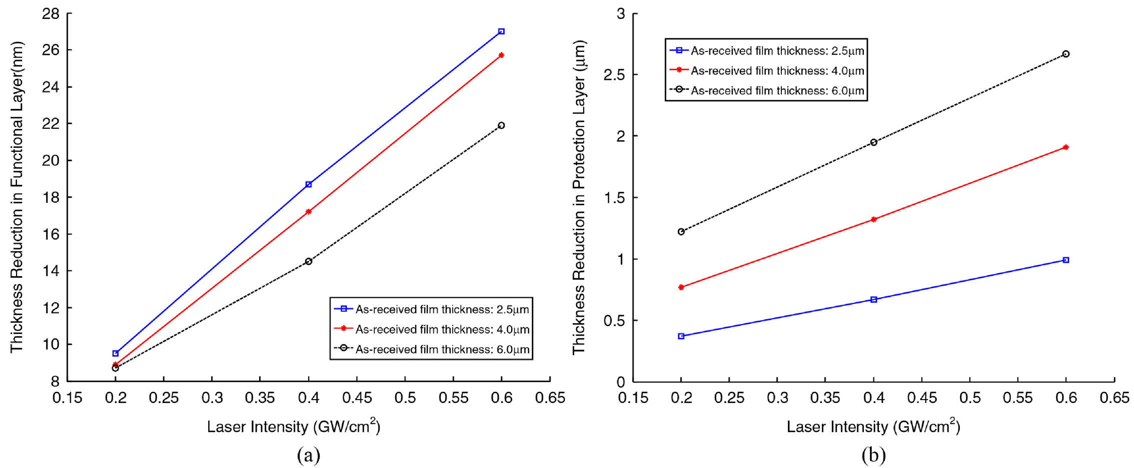

Fig. 9. The thickness reduction in functional Au layer (a) and the protection parylene layer (b) with the increase of as-received parylene thickness and applied laser intensities. The thickness of as-received Au layer is 0.2 μm.

TABLE I
TOTAL STRAIN ENERGY IN FUNCTIONAL AU LAYER

Total strain energy absorbed by Au: K (%)	Laser intensity (GW/cm^2)									
0.2	0.4	0.6								
Strain energy (J)	Strain energy (J)	Strain energy (J)								
in Parylene	In Au	K	in Parylene	In Au	K	in Parylene	In Au	K		
Single parylene thickness (μm)	2.5	0.17	5.6E-3	3.3%	0.28	8.4E-3	3.0%	0.40	12E-3	3.0%
4.0	0.14	3.3E-3	2.3%	0.25	5.0E-3	2.0%	0.38	6.6E-3	1.8%	
6.0	0.11	0.9E-3	0.9%	0.23	2.6E-3	1.1%	0.35	3.8E-3	1.1 %	

the Von Mises over the entire laminates increases, but also the stress discontinuity reaches its maximum at 15th ns, when the delamination and fracture of functional layer are most likely to occur. At the end of the plastic deformation, the shockwave diminishes and the stress relaxation reduces the overall stress and stress discontinuity so that the residual stress concentration across the parylene–Au interface is reduced. In Fig. 8(c), it demonstrates that the overall stress and stress discontinuity increase with the applied laser intensities. There exists stress drop along the thickness direction in the top layer of the parylene, which also increases with the laser intensity. The stress drop helps to mitigate the stress concentration in the metallic layer. Fig. 8(d) reveals that the increase of the parylene thickness contributes to more decrease in the stress discontinuity than that in the overall stress, which reduces the possibility of delamination.

One of the critical hypotheses in this forming technology presumes that most of shockwave energy will be absorbed by the protection parylene layer to minimize the degradation of functional layer. Since the shockwave energy will primarily transform into kinetic energy for material motions and total plastic strain energy stored in the materials, it is expected to find the significant thickness reduction in the protection parylene layer as the indicator of large plastic strains. By FEM simulations, Fig. 9 shows that the thickness reduction in parylene and Au layer both increase with the applied laser intensity approximately in the linear relationship. Also, with the increase of as-received parylene thickness, the thickness reduction of Au layer decreases while that of the parylene layer increases, which again validates that the shockwave energy absorbed by the parylene increases with its thickness. The thickness reductions of the functional layer and the parylene layer need to be controlled in a range to avoid the fracture of structures.

In Table I, it shows that the total strain energy distributed in functional Au layer and protection parylene layer increases with the applied laser intensity and decreases with the parylene thickness. Not only the absolute value of strain energy in Au layer, but also its relative percentage in the overall laminates, decreases with the increasing parylene thickness, which again proves the hypothesis of energy absorption and mechanical protection function by parylene layer.

V. CONCLUSION

Laser dynamic forming has demonstrated its capability and potential to be a flexible and scalable top-down integration technology to manufacture 3-D microscale functional structures on those substrates commonly used in MEMS, without the compromise of device functional degradation. It was verified in terms of the morphologies and functions of functional devices and laminated thin films processed by different laser intensities, cushion layer thickness, and microscale features. The effects of these processing conditions have been characterized quantitatively by an experimental observations and finite element analysis. The ductile connection material could sustain large plastic strains without excessive

necking and failure due to the protection by cushion layer. The ability of direct integration was affected by geometry of 3-D substrates, laser intensity, and parylene thickness. The finite element analysis casts some light on the manufacturing process, including spatial distribution of plastic stress and strain concentration, total strain energy in the heterogeneous materials and stress discontinuity along their interface, which could be further improved to optimize the manufacturing process.

References

[1] P.-J. Chen, S. Saati, R. Varma, M. S. Humayun, and Y.-C. Tai, "Wireless intraocular pressure sensing using microfabricated minimally invasive flexible-coiled LC sensor implant," *J. Microelectromech. Syst.*, vol. 19, no. 4, pp. 721–734, 2010.

[2] Y.-J. Yang, M.-Y. Cheng, S.-C. Shih, X.-H. Huang, C.-M. Tsao, F.-Y. Chang, and K.-C. Fan, "A 32 x 32 temperature and tactile sensing array using PI-copper films," *Int. J. Adv. Manuf. Technol.*, vol. 46, nos. 9–12, pp. 945–956, 2010.

[3] S.-I. Na, S.-S. Kim, J. Jo, and D.-Y. Kim, "Efficient and flexible ITO-free organic solar cells using highly conductive polymer anodes," *Adv. Mater.*, vol. 20, no. 21, p. 4061, 2008.

[4] Y. K. Yoon, J. H. Park, and M. G. Allen, "Multidirectional UV lithography for complex 3-D MEMS structures," *J. Microelectromech. Syst.*, vol. 15, no. 5, pp. 1121–1130, 2006.

[5] M. Mastrangeli, S. Abbasi, C. Varel, C. Van Hoof, J.-P. Celis, and K. F. Bohringer, "Self-assembly from milli-to nanoscales: Methods and applications," *J. Micromech. Microeng.*, vol. 19, no. 8, p. 083001, 2009.

[6] T. Xu, J. Rohozinski, W. Zhao, E. Moorefield, A. Atala, and J. J. Yoo, "Inkjet gene printing: A novel approach to achieve gene modified cells for tissue engineering," *Tissue Eng. A*, vol. 14, no. 5, pp. 869–870, 2008.

[7] R. J. Jackman, S. T. Brittain, A. Adams, H. Wu, M. G. Prentiss, S. Whitesides, and G. M. Whitesides, "Three-dimensional metallic microstructures fabricated by soft lithography and microelectrodeposition," *Langmuir*, vol. 15, no. 3, pp. 826–836, 1999.

[8] H. Schift, "Nanoimprint lithography: An old story in modern times? A review," *J. Vacuum Sci. Technol. B*, vol. 26, no. 2, pp. 458–480, 2008.

[9] J. Yeom and M. A. Shannon, "Detachment lithography of photosensitive polymers: A route to fabricating three-dimensional structures," *Adv. Funct. Mater.*, vol. 20, no. 2, pp. 289–295, 2010.

[10] H. C. Ko, G. Shin, S. Wang, M. P. Stoykovich, J. W. Lee, D. H. Kim, J. S. Ha, Y. Huang, K. C. Hwang, and J. A. Rogers, "Curvilinear electronics formed using silicon membrane circuits and elastomeric transfer elements," *Small*, vol. 5, no. 23, pp. 2703–2709, 2009.

[11] J. Veerbeek, D. N. Reinhoudt, and J. Huskens, "Layer-by-layer assembly using host–guest interactions," in*Multilayer Thin Films: Sequential Assembly of Nanocomposite Materials*, 2nd ed. New York, NY, USA: Wiley, 2012, pp. 83–97.

[12] Z. Liu, D. G. Bucknall, and M. G. Allen, "Inclined nanoimprinting lithography for 3D nanopatterning," *Nanotechnology* vol. 22, no. 22, p. 225302, 2011.

[13] H. Gao and G. J. Cheng, "Laser-induced high-strain-rate superplastic 3-D microforming of metallic thin films," *J. Microelectromech. Syst.*, vol. 19, no. 2, pp. 273–281, 2010.

[14] R. Fabbro, J. Fournier, P. Ballard, D. Devaux, and J. Virmont, "Physical study of laser-produced plasma in confined geometry," *J. Appl. Phys.*, vol. 68, no. 2, pp. 775–784, 1990.

[15] H. Kim, S. A. Hambir, and D. D. Dlott, "Shock compression of organic polymers and proteins: Ultrafast structural relaxation dynamics and energy landscapes," *J. Phys. Chem. B*, vol. 104, no. 17, pp. 4239–4252, 2000.

[16] H. B. Huang and F. Spaepen, "Tensile testing of free-standing Cu, Ag and Al thin films and Ag/Cu multilayers," *Acta Mater.*, vol. 48, no. 12, pp. 3261–3269, 2000.

[17] H. D. Espinosa, B. C. Prorok, and M. Fischer, "A methodology for determining mechanical properties of freestanding thin films and MEMS materials," *J. Mech. Phys. Solids*,vol. 51, no. 1, pp. 47–67, 2003.

[18] N. S. Lu, X. Wang, Z. Suo, and J. Vlassak, "Metal films on polymer substrates stretched beyond 50%," *Appl. Phys. Lett.*, vol. 91, no. 22, p. 221909, 2007.

[19] R. M. Niu, G. Liu, C. Wang, G. Zhang, X. D. Ding, and J. Sun, "Thickness dependent critical strain in submicron Cu films adherent to polymer substrate," *Appl. Phy. Lett.*, vol. 90, no. 16, p. 161907, 2007.

[20] O. Akogwu, D. Kwabi, A. Munhutu, T. Tong, and W. O. Soboyejo, "Adhesion and cyclic stretching of Au thin film on poly(dimethylsiloxane) for stretchable electronics," *J. Appl. Phys.*, vol. 108, no. 12, p. 123509, 2010.

[21] N. S. Lu, Z. G. Suo, and J. J. Vlassak, "The effect of film thickness on the failure strain of polymer-supported metal films," *Acta Mater.*, vol. 58, no. 5, pp. 1679–1687, 2010.

[22] E. Martines, K. Seunarine, H. Morgan, N. Gadegaard, C. D. W. Wilkinson, and M. O. Riehle, "Air-trapping on biocompatible nanopatterns," *Langmuir*, vol. 22, no. 26, pp. 11230–11233, 2006.

[23] G. M. Kappell, J. P. Grover, and T. H. Chrzanowski, "Micro-scale surface-patterning influences biofilm formation," *Electron. J. Biotechnol.*, vol. 12, no. 3, pp. 1–8, 2009.

[24] Z. Burton and B. Bhushan, "Hydrophobicity, adhesion, and friction properties of nanopatterned polymers and scale dependence for micro- and nanoelectromechanical systems," *Nano Lett.*, vol. 5, no. 8, pp. 1607–1613, 2005.

[25] V. E. Ferry, M. A. Verschuuren, H. B. T. Li, E. Verhagen, R. J. Walters, R. E. I. Schropp, H. A. Atwater, and A. Polman, "Light trapping in ultrathin plasmonic solar cells," *Opt. Express*, vol. 18, no. 13, pp. A237–A245, 2010.

[26] H. Yu, L. Ai, M. Rouhanizadeh, D. Patel, E. S. Kim, and T. K. Hsiai, "Flexible polymer sensors for in vivo intravascular shear stress analysis," *J. Microelectromech. Syst.*, vol. 17, no. 5, pp. 1178–1186, 2008.

[27] C. G'sell and J. J. Jonas, "Determination of the plastic behaviour of solid polymers at constant true strain rate," *J. Mater. Sci.*, vol. 14, no. 3, pp. 583–591, Mar. 1979.

Huang Gao received the Ph.D. in industrial engineering from Purdue University, West Lafayette, IN, USA, in 2012 and the B.S. and M.S. degrees in mechanical engineering from Shanghai JiaoTong University, Shanghai, China, in 2001 and 2004, respectively. His research focuses on micro-nanoscale fabrication, laser processing, and dynamic deformations. He was with GE Consumer and Industrial, Louisville, KY, USA, until 2007. He currently holds the position of Senior System Development Engineer at Otis Elevator, Louisville, KY, USA.

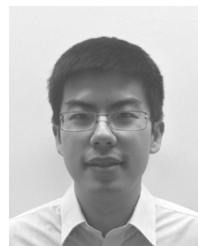

Rui Tang received the B.S. degree from Huazhong University of Science and Technology, Wuhan, China, in 2009 and the M.S. degree from Arizona State University (ASU), Tempe, AZ, USA, in 2011. He is currently pursuing the Ph.D degree at the School of Electrical, Computer and Energy Engineering, ASU. His current research includes the development of MEMS flow sensors, 3-D MEMS packaging and flexible, stretchable and foldable skins with integrated sensors and electronics.

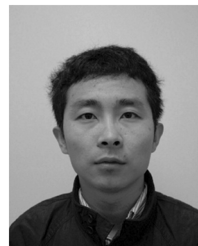

Teng Ma received the B.S. degree in thermal and power engineering from Xi'an Jiaotong University, Shanghai, China, in 2004 and the M.S. degree in mechatronics engineering in University of Electronic Science and Technology of China in 2009. He is currently pursuing the Ph.D degree in mechanical engineering at the School for Engineering of Matter, Transport and Energy, Arizona State University, Tempe, AZ, USA, in the research group of Dr. Hanqing Jiang. His research focuses on buckled stiff thin film on soft substrate for versatile functional materials, including anodes for lithium ion batteries, optical gratings for micro-strain sensors and piezoelectric materials for energy harvesting devices.

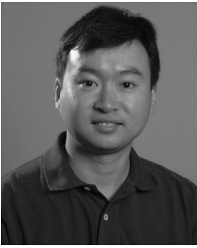

Hanqing Jiang is an Associate Professor of Mechanical and Aerospace Engineering at Arizona State University (ASU), Tempe, AZ, USA. Dr. Jiang received the Ph.D. degree from Tsinghua University, China, in 2001, majoring in solid mechanics, and then worked as a Post-Doctoral Research Associate at the University of Illinois at Urbana-Champaign, Urbana, IL, USA, before joining ASU in 2006. His current research interests are multiphysics modeling and experiments for heterogeneous hard and soft materials.

Hongyu Yu received the B.S. and M.S. degrees from Tsinghua University, China, in 1997 and 2000, respectively, and the Ph.D. degree from the University of Southern California, Los Angeles, CA, USA, in 2005. He holds a joint position between School of Earth and Space Exploration and School of Electrical, Computer and Energy Engineering at Arizona State University, Tempe, AZ, USA. His research focuses on MEMS for Earth and Space applications with interests in micro seismometers, harsh environment sensing, wireless sensing systems, flexible and stretchable electronics and manufacture.

Gary J. Cheng received the Ph.D. degree in mechanical engineering from Columbia University, New York, NY, USA, in 2002. He is an Associate Professor in the School of Industrial Engineering and Mechanical Engineering by courtesy. His current research interests include scalable manufacturing of 0-D–3-D micro/nanostructures, laser matter interaction, and mechanical/physical property enhancement of materials.